*Nonlinear Dynamics* **11:** 189–212, 1996.


# A Finite Element Approach to the Chaotic Motion of Geometrically Exact Rods Undergoing In-Plane Deformations

C. SANSOUR
*Technische Hochschule Darmstadt, Fachgebiet Maschinenelemente und Maschinenakustik, Magdalenenstr. 4, 64289 Darmstadt, Germany*

J. SANSOUR and P. WRIGGERS
*Technische Hochschule Darmstadt, Fachbereich Mechanik, Hochschulstr. 1, 64289 Darmstadt, Germany*

(Received: 10 July 1995; accepted: 24 January 1996)

**Abstract.** The paper is concerned with a hybrid finite element formulation for the geometrically exact dynamics of rods with applications to chaotic motion. The rod theory is developed for in-plane motions using the direct approach where the rod is treated as a one-dimensional Cosserat line. Shear deformation is included in the formulation. Within the elements, a linear distribution of the kinematical fields is combined with a constant distribution of the normal and shear forces. For time integration, the mid-point rule is employed. Various numerical examples of chaotic motion of straight and initially curved rods are presented proving the powerfulness and applicability of the finite element formulation.

**Key words:** Geometric exact rods, finite elements, integration schemes, chaotic motion.

## 1. Introduction

Since the work of Holmes [4], chaotic motion of beams has attracted the interest of many researchers (see, e.g., [5, 7, 8, 10]). In some papers (e.g., [9, 11–13]) the arch has been considered too.

The mentioned papers are based on analytic methods, thus different restrictions in modeling the rod must be taken into account in order for the analysis to be achievable at all. Specifically, the nonlinearities are restricted only to the dominant terms, only first order modes are considered, the load is assumed to have specific forms (sine or cosine functions), and in general the equations of the Euler–Bernoulli rod model are considered where the shear deformation is neglected. Contrasting the above investigations, this paper is aimed at a numerical approach to chaos using the finite element method where, as a first step, the in-plane rod is considered. The advantage of such an approach lies in the following facts:

1. The nonlinearities can be modeled completely due to a geometrically exact description of the rod kinematics.
2. Higher order modes are considered naturally by using a sufficient large number of finite elements.
3. A rod model with first order shear deformation is considered.
4. The load function and the boundary conditions can be practically arbitrary.

Nevertheless, it is our believe that both approaches are complementary and should co-exist. Analytical methods have the important advantage of allowing general conclusions where the problem parameters are not specified a priori, making possible a rigorous understanding of different phenomena.

Although the geometrically exact rod model is well known in the literature (see, e.g., [1, 14, 19, 23]), we will rederive the rod equations by means of the direct approach, namely by considering the rod as a Cosserat line. The approach has the advantage that the model arises as a special case of Cosserat continua which can be generalized to model shells and rods in space as well (see Sansour and Bednarczyk [15]). Some remarks concerning the terminology 'geometrically exact' used in the paper are appropriate. The terminology used means that the strain-displacement relations are considered in complete form without any simplifications. A rod model can be geometrically exact but take only a linear constitutive relation. In general, a finite strain model means more than that; namely, a geometrically exact one where, in addition, finite strain nonlinear constitutive equations are employed. Since the constitutive relations used in this paper are linear, the term 'geometrically exact' is accordingly more appropriate.

Special attention must be devoted to the finite element formulation in order to avoid ill-conditioning and locking phenomena. In this paper a hybrid finite element is developed. The term hybrid is due to the fact that the force terms (normal and shear forces) are taken in a mixed Hellinger–Reissner type formulation using a Legendre transformation. The finite element is characterized by a linear distribution of the kinematical fields and constant force distributions over the element. By that, and in spite of the simplicity of the element formulation, we are able to formulate very robust elements capable to describe finite rotations.

Beyond the element formulation, the time integration procedure plays an important rule. As a first step, the midpoint rule is used here. It was recently proven that this symplectic scheme conserves momentum and moment of momentum (see [22]). The construction and application of an energy-momentum method, that is a method which preserves the energy in a case of a Hamiltonian system, is left for a future report. In this case the configuration space is not a vector space, the mentioned construction is by no means simple and becomes of special interest.

## 2. The Rod Model

In the following we derive the equations of the geometrically exact rod model by a direct approach. The model is well known in the literature (see, e.g., [14, 19]) where it is usually derived by using specific assumptions for the displacement field. Nevertheless, the way we are following has the very important advantage that the method is general enough to apply to rods in three-dimensional space as well as to shells with arbitrary geometry. In each case it is only the Cosserat continuum under consideration which has to be specified. The strain tensors remain, by their definition, the same; only their components differ depending on the underlined continuum. After the formal derivation we simplify the notation which is more appropriate for the special problem considered.

Let $\mathcal{B} \in \mathcal{R}^3$, where $\mathcal{R}$ denotes the real numbers, be a one-dimensional manifold defining a body understood as a one-dimensional continuum. A motion of $\mathcal{B}$ is a map, $\varphi(t)$, $t \in \mathcal{R}$, parametrized by the time $t$ according to $\varphi(t) : \mathcal{B} \to \mathcal{R}^3$, $\varphi(t)\mathcal{B} = \mathcal{B}_t$. In the sense of a reference configuration we identify $\varphi_0 = \varphi$ $(t = t_0)$ with the identity map. For $\mathbf{X} \in \mathcal{B}$ and $\mathbf{x} \in \mathcal{B}_t$ we have $\mathbf{x}(t) = \varphi(\mathbf{X}, t)$. Let further $s$ be coordinate charts in $\mathcal{B}$, which we choose to be attached to the body and at the same time take to be the arc length. The covariant base vectors of the tangent spaces at either configuration are given by

$$\mathbf{G} = \partial \mathbf{X}/\partial s, \qquad \mathbf{g} = \partial \mathbf{x}/\partial s. \tag{1}$$

Accordingly, the *Riemannian* metric is $G = \mathbf{G} \cdot \mathbf{G} = 1$ and $g = \mathbf{g} \cdot \mathbf{g}$ in each configuration respectively, where scalar products of vectors are denoted by a dot. Further, we consider a Cartesian frame denoted by $\mathbf{e}_i$. In the whole paper Latin indices take the values 1, 2, 3. We assume that the plane where the deformation takes place is spanned by the vectors $\mathbf{e}_1$ and $\mathbf{e}_2$. Accordingly $\mathbf{G} \cdot \mathbf{e}_3 = 0$. The normal vector to the tangent space of the rod, $\mathbf{N}$, is given by the relation $\mathbf{N} = \mathbf{G} \times \mathbf{e}_3$. Altogether, the representation holds

$$\mathbf{G} = -\sin\alpha\mathbf{e}_1 + \cos\alpha\mathbf{e}_2, \qquad \mathbf{N} = \cos\alpha\mathbf{e}_1 + \sin\alpha\mathbf{e}_2. \tag{2}$$

$\alpha$, a function of $s$, determines the angle closed between $\mathbf{e}_1$ and $\mathbf{N}$. It defines together with the initial boundary conditions the reference configuration.

The deformation gradient, the gradient of the map $\varphi$, is defined as the tensor product of the two vectors according to

$$\mathbf{F} = \mathbf{g} \otimes \mathbf{G}. \tag{3}$$

It maps the tangent space of $\mathcal{B}$ at the reference configuration to that at the actual configuration. Note that $\mathbf{F}$ is one-dimensional by the fact that the tangent spaces themselves are one-dimensional.

The understanding that $\mathcal{B}$ is a Cosserat line is connected with the fact that we attach to $\mathcal{B}$ two independent fields; a displacement and a rotational field. The first has been already introduced by means of the map $\varphi$. Explicitly we define the displacement field according to

$$\mathbf{u} = \mathbf{x} - \mathbf{X}. \tag{4}$$

By denoting partial derivatives by a comma we obtain with (1) and (4)

$$\mathbf{g} = \mathbf{G} + \mathbf{u}_{,s} \tag{5}$$

and with (3)

$$\mathbf{F} = (\mathbf{G} + \mathbf{u}_{,s}) \otimes \mathbf{G}. \tag{6}$$

We now consider the rotation field $\mathbf{R} \in SO(3)$ where $SO(3)$ is the group of orthogonal tensors with positive determinant. Since we are considering in-plane rotations, the direction of the rotation vector is fixed to $\mathbf{e}_3$. The only open parameter is its absolute value which we denote by $\omega$. In this case the rotation tensor has the closed form representation

$$\mathbf{R} = \cos\omega(\mathbf{e}_1 \otimes \mathbf{e}_1 + \mathbf{e}_2 \otimes \mathbf{e}_2) - \sin\omega(\mathbf{e}_1 \otimes \mathbf{e}_2 - \mathbf{e}_2 \otimes \mathbf{e}_1) + \mathbf{e}_3 \otimes \mathbf{e}_3. \tag{7}$$

Since $\mathbf{R}^T\mathbf{R} = \mathbf{1}$, the product $\mathbf{R}^T\mathbf{R}_{,s}$ is skew symmetric. We denote the corresponding axial vector by $\mathbf{k}$.

Having established the one-dimensional deformation gradient and introduced the rotation tensor relevant to our problem, we are now in a situation to derive the strain measures by applying the direct method of a Cosserat line. The method has been successfully used to derive geometrically exact shell models (see [15]). The strain measures of the Cosserat continuum are: The first Cosserat deformation tensor (the stretch tensor)

$$\mathbf{U} := \mathbf{R}^T\mathbf{F} \tag{8}$$

and the second Cosserat strain tensor (the curvature tensor)

$$\mathbf{K} := -\mathbf{k} \otimes \mathbf{G}. \tag{9}$$

Due to the fact that the Cosserat continuum is assumed to be one-dimensional and restricted to in-plane deformations, only the following components of **u**, **U**, **K** are different from zero

$$\mathbf{u} = u_1\mathbf{e}_1 + u_2\mathbf{e}_2 \tag{10}$$

$$\mathbf{U} = U_{11}\mathbf{G}\otimes\mathbf{G} + U_{13}\mathbf{G}\otimes\mathbf{N} \tag{11}$$

$$\mathbf{K} = \kappa\mathbf{e}_3\otimes\mathbf{G}. \tag{12}$$

Note that the decomposition of the displacement vector **u** is naturally carried out with respect to a Cartesian frame. Contrasting this, the strain tensor **U**, **K** is defined with respect to the natural orthonormal frame given by the set $(\mathbf{G}, \mathbf{e}_3, \mathbf{N})$ allowing for a natural and direct physical interpretation. The validity of the above decompositions is verified by straightforward calculations which we omit. Explicitly we get using (6–12):

$$U_{11} = \cos\omega + \cos(\alpha+\omega)u_{1,s} + \sin(\alpha+\omega)u_{2,s} \tag{13}$$

$$U_{13} = -\sin\omega - \sin(\alpha+\omega)u_{1,s} + \cos(\alpha+\omega)u_{2,s} \tag{14}$$

$$\kappa = \omega_{,s}. \tag{15}$$

Note that shear deformation is included in this model and is not set to zero.

It is these strain-displacement relations that motivate the terminology 'geometrically exact description' since the whole geometric nonlinearity is taken into account. Analytical methods as applied to structural dynamics and which can be found in the literature cited in the introduction are based on simplified versions of these strain-displacement relations, the derivation of which can be carried out by applying severe restrictions and assumptions concerning the admissible deformations.

## 3. The Dynamical Formulation

We assume now the existence of an internal energy function per unit length depending quadratically on the strain measures **U**, **K**. Accordingly, the force and moment tensors are given by

$$\boldsymbol{n} = \frac{\partial\psi}{\partial\mathbf{U}}, \tag{16}$$

$$\mathbf{m} = \frac{\partial\psi}{\partial\mathbf{K}}. \tag{17}$$

Using the same decompositions as in (11), (12) we obtain

$$\boldsymbol{n} = n_{11}\mathbf{G}\otimes\mathbf{G} + n_{13}\mathbf{G}\otimes\mathbf{N}, \tag{18}$$

$$\mathbf{m} = m\mathbf{e}_3\otimes\mathbf{G}. \tag{19}$$

Explicitly we define $\psi$ such that the linear relations hold

$$n_{11} = EA(U_{11} - 1), \tag{20}$$

$$n_{13} = GAU_{13}, \tag{21}$$

$$m = EI\kappa. \tag{22}$$

The interpretations are of course valid that $E$ is Young's modulus, $G$ the shearing modulus, $A$ the section area, and $I$ the moment of inertia. In addition we consider the kinetic energy formulated as

$$T = \frac{1}{2}\,(\rho A\dot{\mathbf{u}} \cdot \dot{\mathbf{u}} + \rho I\dot{\omega}^2). \tag{23}$$

Here $\rho$ defines an adequately defined density. At this stage it is useful to simplify the notation by introducing the force and strain vectors

$$\mathbf{n} = \begin{Bmatrix} n_{11} \\ n_{13} \end{Bmatrix}, \qquad \varepsilon = \begin{Bmatrix} (U_{11}(\mathbf{u},\omega) - 1) \\ U_{13}(\mathbf{u},\omega) \end{Bmatrix}, \tag{24}$$

where it is understood that the relations (13), (14) have to be employed. The stored energy function is written in decoupled form as $\psi = \psi_1(\varepsilon) + \psi_2(\kappa)$. From the numerical point of view and in order to avoid locking phenomena and to construct robust finite elements, it is useful to convert that part of the internal energy related to the strains $\varepsilon$ into the complementary one $\tilde{\psi}(\mathbf{n})$ using a Legendre transformation. The latter reads

$$\psi_1(\varepsilon) + \tilde{\psi}(\mathbf{n}) = \mathbf{n} \cdot \varepsilon. \tag{25}$$

After these preparations we are in a situation to formulate a D'Alembert-like principle to provide a basis for the finite element formulation in the next section:

$$\delta T = \delta\Psi_{\text{int}} + \delta W_{\text{ext}} = 0, \tag{26}$$

where $\delta\Psi_{\text{int}}$, $\delta W_{\text{ext}}$ denote the internal and the external virtual work, respectively. Explicitly we have using (25)

$$\Psi_{\text{int}} = \int_{\mathcal{B}} (\psi_1(\varepsilon) + \psi_2(\kappa))\,\mathrm{d}s = \int_{\mathcal{B}} (\mathbf{n} \cdot \varepsilon - \tilde{\psi}(\mathbf{n}) + \psi_2(\kappa))\,\mathrm{d}s, \tag{27}$$

$$\delta W_{\text{ext}} = \int_{\mathcal{B}} (\mathbf{p} \cdot \delta\mathbf{u} + M\delta\omega)\,\mathrm{d}s + (\mathbf{p} \cdot \delta\mathbf{u} + M \cdot \delta\omega)|_{\partial\mathcal{B}}\,. \tag{28}$$

Here, $\mathbf{p}$ and $\mathbf{M}$ describe the external forces and moments (possibly deformation and velocity dependent) in the field as well as at the boundaries of the rod which are denoted by $\partial\mathcal{B}$. The forces are admitted to depend on the velocities to take into account possible dissipation. Making use of (23), (26–28) as well as applying Gauss theorem we end up with the variational form

$$\begin{aligned} J(\mathbf{u},\omega,\mathbf{n},\delta\mathbf{u},\delta\omega,\delta\mathbf{n}) &= \int_{\mathcal{B}} \rho(A\ddot{\mathbf{u}} \cdot \delta\mathbf{u} + I\ddot{\omega}\delta\omega)\,\mathrm{d}s \\ &- \int_{\mathcal{B}} \left[\delta\mathbf{n} \cdot \varepsilon(\mathbf{u},\omega) + \mathbf{n} \cdot \frac{\partial\varepsilon(\mathbf{u},\omega)}{\partial\mathbf{u}}\,\delta\mathbf{u} + \mathbf{n} \cdot \frac{\partial\varepsilon(\mathbf{u},\omega)}{\partial\omega}\,\delta\omega - \frac{\partial\tilde{\psi}(\mathbf{n})}{\partial\mathbf{n}}\,\delta\mathbf{n} + \frac{\partial\psi_2(\omega)}{\partial\omega}\,\delta\omega\right]\mathrm{d}s \\ &+ \int_{\mathcal{B}} (\mathbf{p} \cdot \delta\mathbf{u} + M\delta\omega)\,\mathrm{d}s + (\mathbf{p} \cdot \delta\mathbf{u} + M\delta\omega)|_{\partial\mathcal{B}} \\ &= 0. \end{aligned} \tag{29}$$

Note, that $\psi_2(\omega)$ means that $\kappa$ is replaced in $\psi_2$ using (15).

## 4. The Finite Element Approach

In this section the finite element formulation of the theory presented above is developed on the ground of the functional (29). The finite element will be of the hybrid type, that is the components of $\mathbf{n}$ are eliminated at the element level. A two-node element with linear kinematical fields and constant force $\mathbf{n}$ (normal and shear components) is considered.

Geometric quantities describing the geometry of the rod are considered exactly at the Gauss integration points. All kinematical fields are interpolated using linear interpolation functions. The procedure is standard, hence details are omitted. The interpolation procedure is documented in the relation

$$\begin{Bmatrix} \mathbf{u} \\ \omega \end{Bmatrix} = \mathbf{E}\mathbf{u}^e, \tag{30}$$

where $\mathbf{u}^e$ denotes the degrees of freedom of the element and $\mathbf{E}$ is then a $3 \times 6$ matrix which depends on the shape functions.

We assume a constant interpolation for $\mathbf{n}$ which is discontinuous over the elements and can be eliminated at the element level. The interpolation yields

$$\mathbf{n}(\xi) = \begin{Bmatrix} S_1 \\ S_2 \end{Bmatrix}, \qquad \mathbf{n} = \mathbf{D}\mathbf{S}^e. \tag{31}$$

Here, $S_1, S_2, \ldots$ are some constants determining the force field within the element which are gathered in the vector $\mathbf{S}^e$. $\mathbf{D}$ is then a $2 \times 2$ matrix. The stress interpolations used guarantee, as intensive numerical experiments show, that the numerical solutions are free of ill-conditioning in the range of thin rods which is well known as locking phenomena.

For the numerical integration, two Gaussian integration points are used (full numerical integration).

## 5. The Solution Procedure

We denote all degrees of freedom of the rod ($\mathbf{u}$ and $\omega$) by $\boldsymbol{u}$. The elaboration of the functional (29) by introducing the interpolation functions and carrying out the numerical integration leads to the following set of algebraic and ordinary differential equations:

$$\sum_1^N \mathbf{A}^e\mathbf{S}^e = \sum_1^N \mathbf{b}^e(\boldsymbol{u}) \tag{32}$$

$$\sum_1^N [\mathbf{M}^e\ddot{\boldsymbol{u}}^e + \mathbf{C}^e\dot{\boldsymbol{u}}^e + \mathbf{B}^e(\boldsymbol{u})\mathbf{S}^e + \mathbf{K}^e\boldsymbol{u}^e] = \sum_1^N \mathbf{q}^e(\boldsymbol{u}). \tag{33}$$

The upper index $e$ denotes quantities defined at the element level. $N$ is the number of elements involved. $\mathbf{A}^e$, $\mathbf{M}^e$, $\mathbf{C}^e$, $\mathbf{K}^e$ are quadratic matrices. $\mathbf{A}^e$ is constant by the linearity of the constitutive equations (20), (21) and has the dimension $2 \times 2$, $\mathbf{M}^e$ represents the mass matrix and has the dimension $6 \times 6$, and $\mathbf{C}^e$ is the damping matrix stemming from velocity dependent forces, where we assume the linear relation between damping forces and velocities,

the damping coefficient will be denoted $d$. Hence, $\mathbf{C}^e$ is constant and has the dimension $6 \times 6$ too. The vector $\mathbf{b}^e$ depends in a nonlinear fashion on the kinematical field $\boldsymbol{u}$. The nonlinearity has a purely geometric source and reflects the nonlinear relations (13, 14). The matrix $\mathbf{K}$ stems from the bending stiffness. It is constant due to the linearity of relation (15). The matrix $\mathbf{B}^e$ is nonquadratic. It has the dimension $2 \times 6$. Furthermore, the relation holds

$$\frac{\partial \mathbf{b}^e(\boldsymbol{u})}{\partial \boldsymbol{u}} = \mathbf{B}^{eT}(\boldsymbol{u}). \tag{34}$$

The solution procedure goes as follows. Since the unknowns $\mathbf{S}^e$ are assumed to be discontinuous over the elements, equation (32) can be solved at the element level

$$\mathbf{S}^e = \mathbf{A}^{e-1}\mathbf{b}^e(\boldsymbol{u}) \tag{35}$$

which can be introduced in (33) to eliminate $\mathbf{S}^e$. The resulting nonlinear equation reads

$$\sum_N [\mathbf{M}^e \ddot{\boldsymbol{u}}^e + \mathbf{C}^e \dot{\boldsymbol{u}}^e + \mathbf{B}^e \mathbf{A}^{e-1} \mathbf{b}^e(\boldsymbol{u}) + \mathbf{K}^e \boldsymbol{u}^e] = \sum_1^N \mathbf{q}^e(\boldsymbol{u}) \tag{36}$$

which can be written in the standard form at the global level

$$\mathbf{M}\ddot{\boldsymbol{u}} + \mathbf{C}\dot{\boldsymbol{u}} + \mathbf{k}(\boldsymbol{u}) = \mathbf{0}. \tag{37}$$

$\mathbf{k}$ is the vector of all nodal internal and external forces which depends nonlinearily on the kinematical field $\boldsymbol{u}$.

Let $n$ denote a converged time step with the known solution $\boldsymbol{u}_n$ and $\dot{\boldsymbol{u}}_n$, $n+1$ the next time step with the unknown solution $\boldsymbol{u}_{n+1}$ and $\Delta T$ the time increment. The solution of the above nonlinear ordinary differential equation is accomplished by using an implicit mid-point rule

$$\mathbf{M}\left(\frac{\dot{\boldsymbol{u}}_{n+1} - \dot{\boldsymbol{u}}_n}{\Delta T}\right) + \mathbf{C}\dot{\boldsymbol{u}}_{n+(1/2)} + \mathbf{k}(\boldsymbol{u}_{n+(1/2)}) = \mathbf{0}. \tag{38}$$

With the following approximations

$$\boldsymbol{u}_{n+1} = \boldsymbol{u}_n + \Delta \boldsymbol{u}, \tag{39}$$

$$\boldsymbol{u}_{n+(1/2)} = \boldsymbol{u}_n + \frac{\Delta \boldsymbol{u}}{2}, \tag{40}$$

$$\dot{\boldsymbol{u}}_{n+(1/2)} = \frac{\Delta \boldsymbol{u}}{\Delta T}, \tag{41}$$

$$\dot{\boldsymbol{u}}_{n+(1/2)} = \frac{\dot{\boldsymbol{u}}_{n+1} + \dot{\boldsymbol{u}}_n}{2}, \tag{42}$$

equation (38) can be rewritten as

$$\mathbf{M}\left(\frac{2}{(\Delta T)^2}\Delta \boldsymbol{u} - \frac{2}{\Delta T}\dot{\boldsymbol{u}}_n\right) + \mathbf{C}\frac{1}{\Delta T}\Delta \boldsymbol{u} + \mathbf{k}\left(\boldsymbol{u}_n + \frac{1}{2}\Delta \boldsymbol{u}\right) = \mathbf{0}. \tag{43}$$

The last relation constitutes a nonlinear equation for $\Delta \boldsymbol{u}$ which is solved using Newton's method.

| Material constants | Geometry |
|---|---|
| Young's modulus.....E=1.2E4 | Cross section.....Q=1× 1 |
| Poison ratio.....$\nu$=0.2 | Length.....L=10 |
| Density.....$\rho$=1.0E-6 | |
| Damping.....d= 5.0E-4 | |

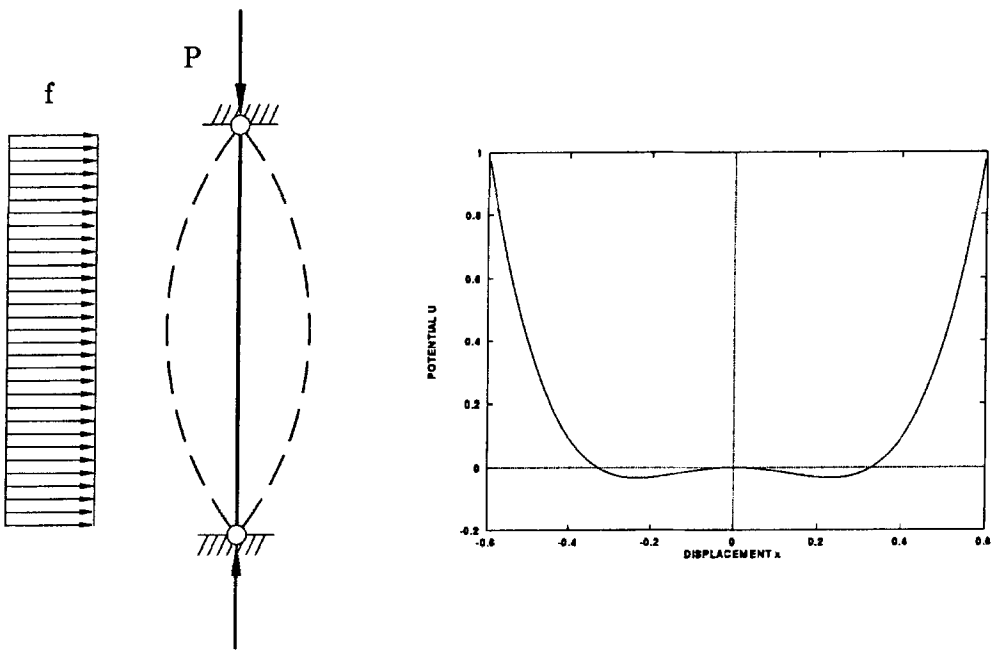


*Figure 1.* The excited buckled beam model with the used data in the FE-calculations.

## 6. Numerical Examples

In the following, nonlinear oscillations of a buckled beam (excited harmonically by a transverse, constant load) as well as nonlinear oscillations of shallow arches (excited harmonically by a concentrated load) will be discussed in detail including chaotic motions.

### 6.1. The Harmonically Excited Buckled Beam

A beam (10 length units) is subjected to an axial load, $P$, greater than its Euler buckling load which results in an axial displacement $\Delta u = 0.11$. It is fixed in simple supports which restricts its axial motion. A transverse, constant load distribution of the form $f = F\cos(\omega t)$ was then applied. The model is shown in Figure 1.

In varying the forcing amplitude and forcing frequency the buckled beam can undergo chaotic vibrations of different types.

- Due to soft-spring characteristics the buckled beam may exhibit period-doubling cascades to chaos in one of the potential wells.

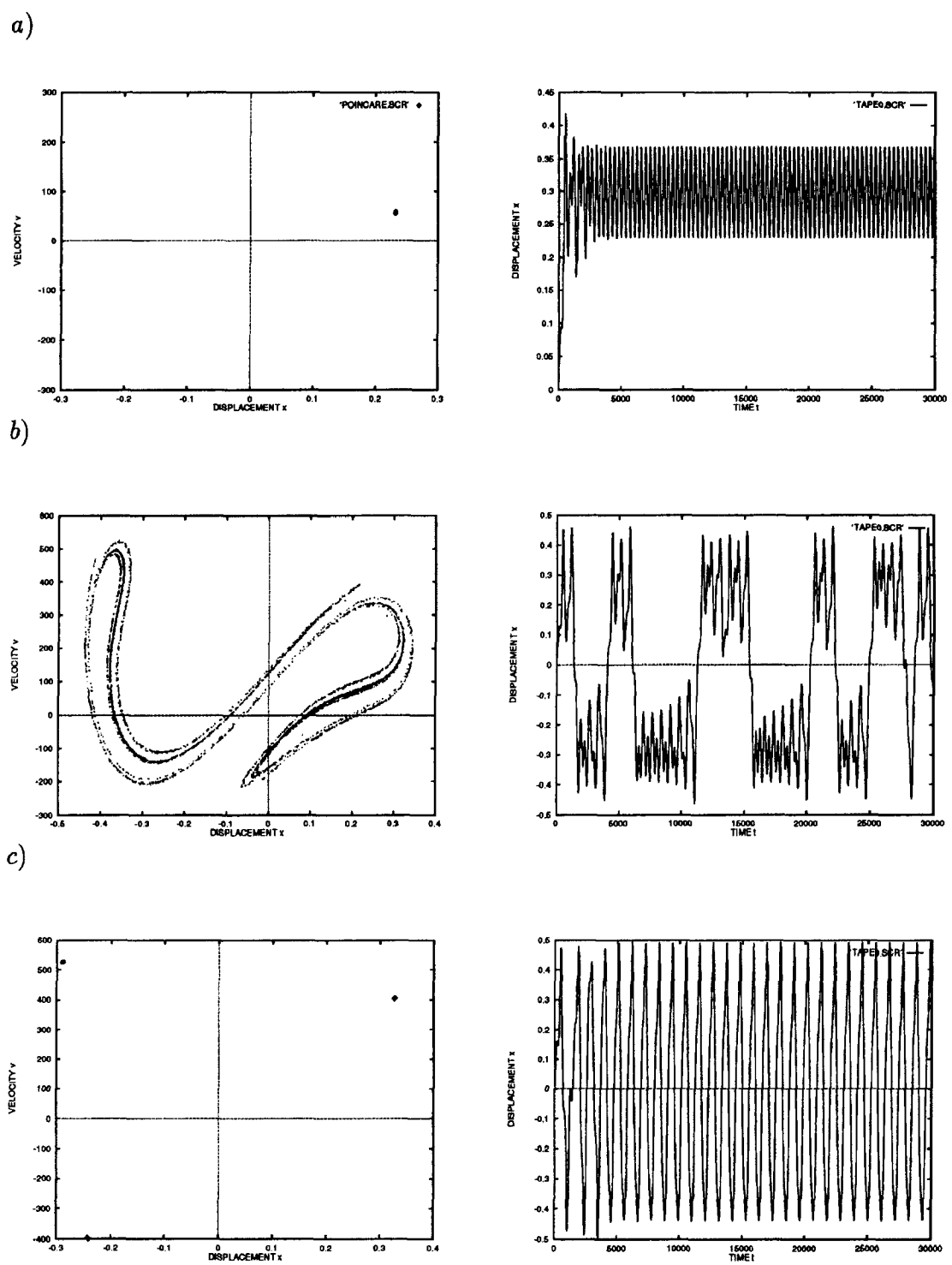


*Figure 2.* Poincaré plots and $(x, t)$-diagrams by varying $F$ from (0.4–2). Chaotic motions in the transition zone between the small orbit and the large one interrupted by an odd-period motion. (a) Small orbit around the right equilibrium position. (b) Chaotic motion around both stable equilibria. (c) Globally three-period motion.

d)

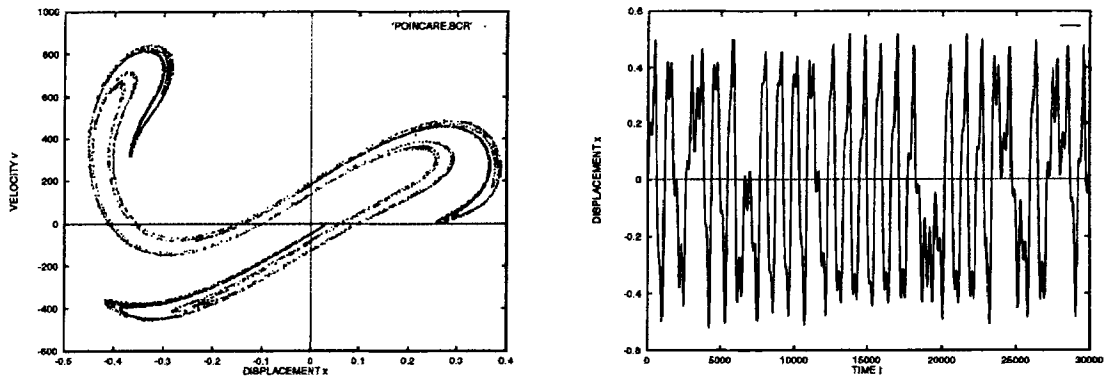


e)

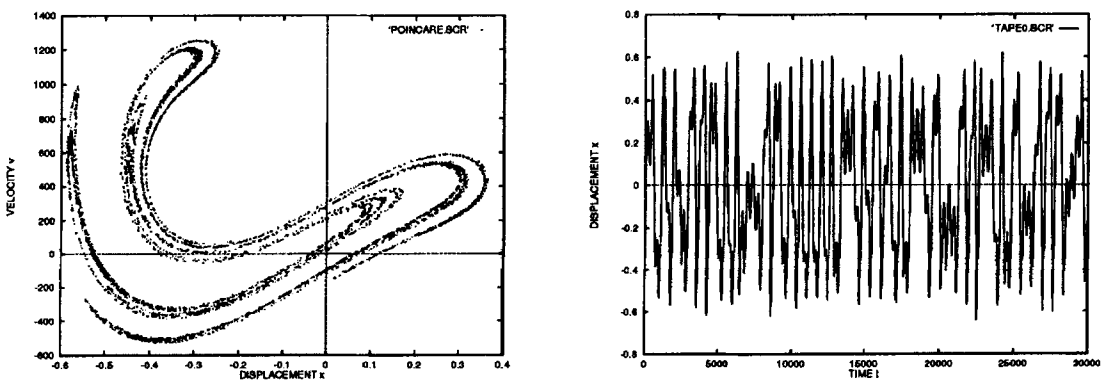


f)

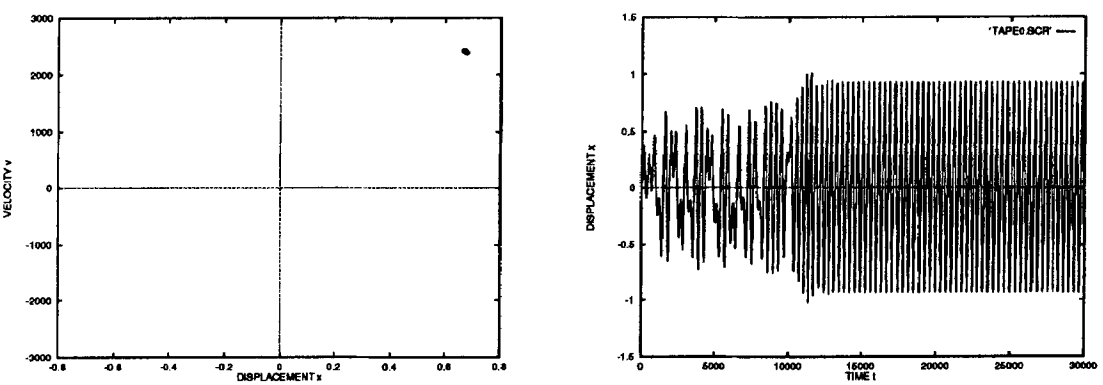


*Figure 2.* (Continued) (d) Chaotic motion due to period-doubling of the odd-period motion. (e) Globally chaotic motion. (f) Periodic motion (large orbit) around all the equilibria.

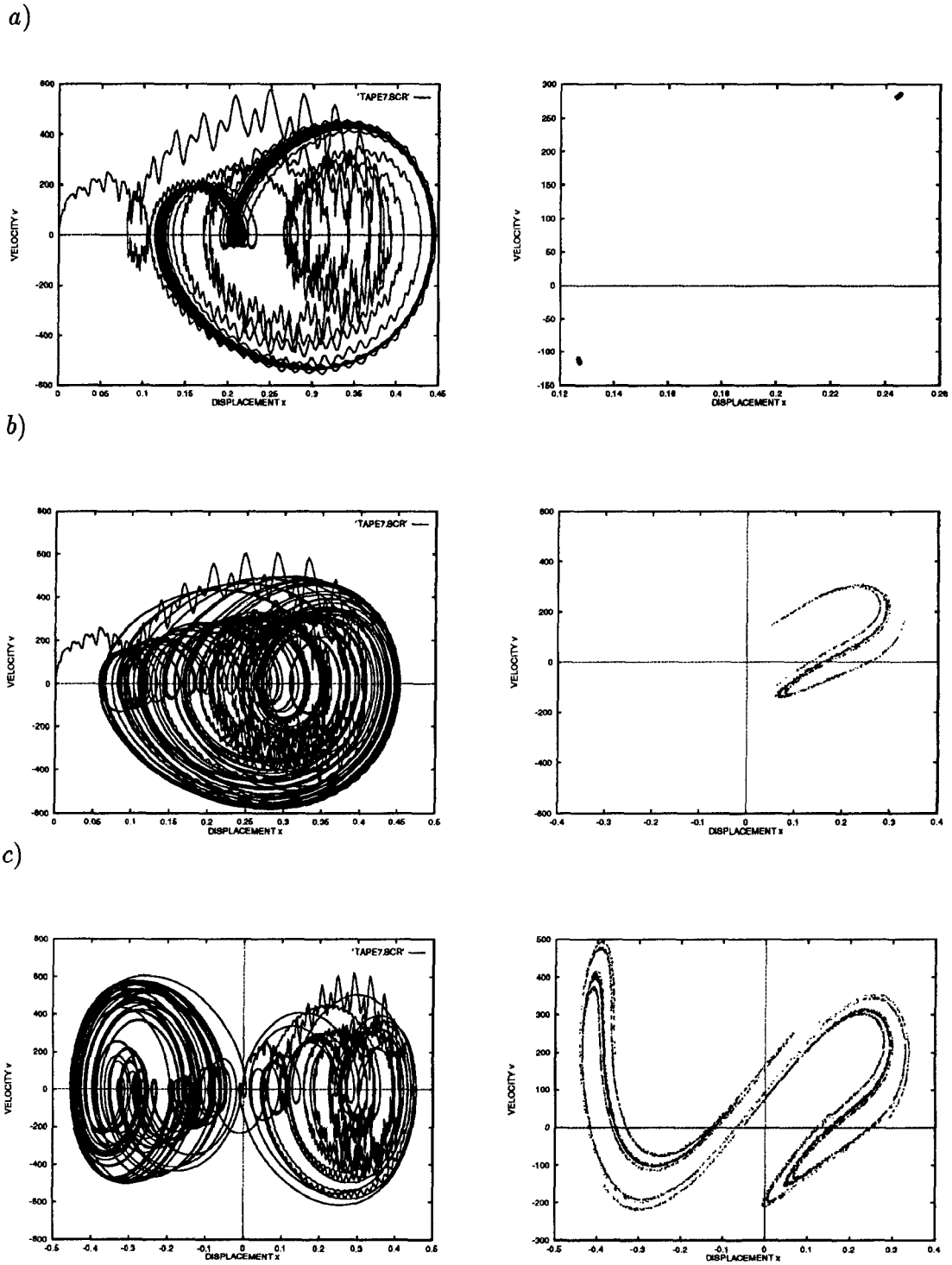


*Figure 3.* Phase space diagrams and Poincaré plots for fixed $F$ but different $\omega$ from (3.4E3–4.2E3). (a) Two-period motion. (b) Locally chaotic due to the period-doubling of (a). (c) Chaotic around both equilibrium positions.

d)

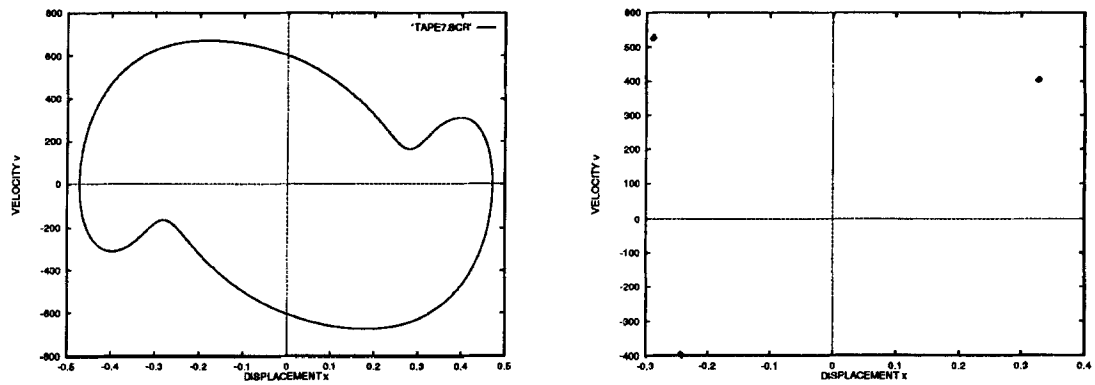


e)

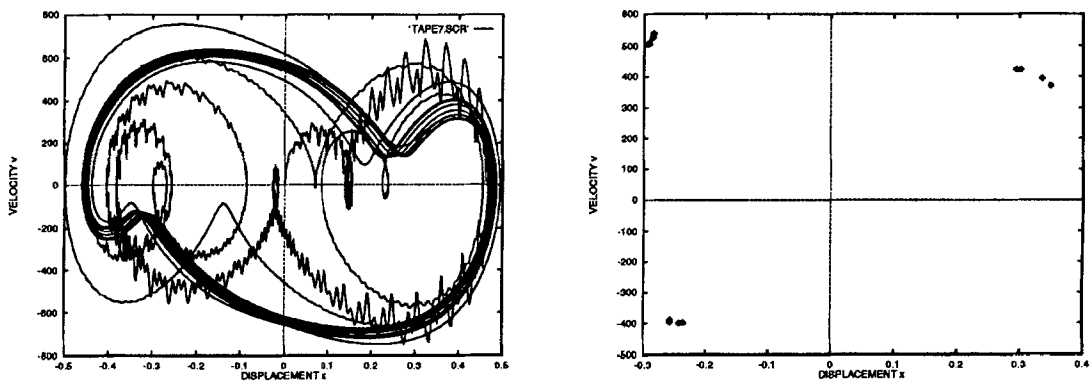


f)

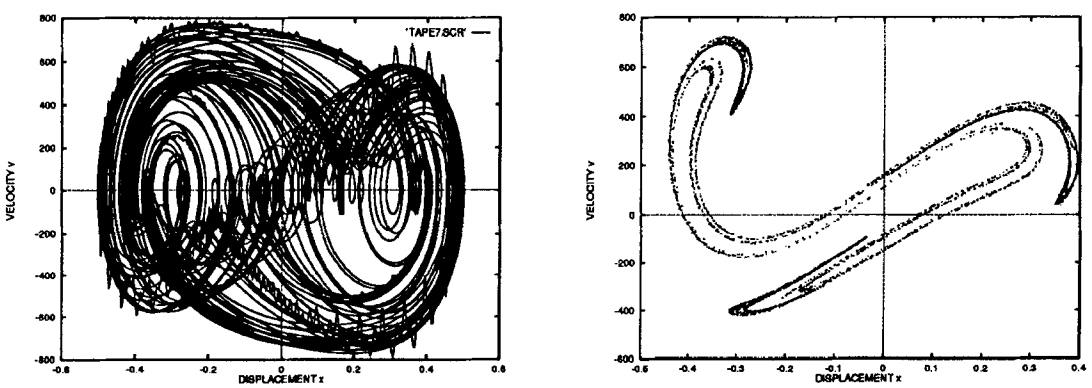


*Figure 3.* (Continued) (d) Three-period motion. (e) Doubling of the three-period motion. (f) Globally chaotic motion due to the period-doubling of (e).

- The beam may vibrate chaotically in an irregular manner between the equilibrium positions. This can happen either because of the symmetry of the two potential wells with soft-spring characteristics, or due to period-doubling cascades of the globally odd subharmonic oscillations.
- Transient chaos between the regular motions.

Figure 2 shows Poincaré plots and displacement-time diagrams for the nonlinear oscillations of the beam by varying the forcing amplitude $F$ between (0.4–2) while the forcing frequency $\omega$ was fixed to 3.5E3. The distance of the Poincaré sections was taken to equal the forcing period; recall that a Poincaré plot is the projection of $(x, \dot{x}, t)$-trajectory points for certain $t_s$ onto the $(x, \dot{x})$-plane. Ten linear finite elements were used. Mid-displacements and mid-velocities are plotted next after the high frequency motions have died out due to dissipation: (2a) $F = 0.4$, (2b) $F = 0.6$, (2c) $F = 0.7$, (2d) $F = 0.9$, (2e) $F = 1.5$, (2f) $F = 2.0$.

Figure 3 shows phase portraits with their corresponding Poincaré sections and the doubling of figures which lead to various chaotic motions by changing the forcing frequency between (3.4E3–4.2E3) while the forcing amplitude was fixed to 0.7: (3a) $\omega = 4.2$E3, (3b) $\omega = 4.05$E3, (c) $\omega = 4.0$E3, (3d) $\omega = 3.6$E3, (3e) $\omega = 3.55$E3, (3f) $\omega = 3.4$E3.

Again ten finite elements were used to model the beam. In order to have a comparison with a low dimensional analysis one must take a low number of elements to model the beam, but it must be noticed that the use of different number of elements (less than ten) produces different dynamical responses of the beam. This point will be discussed in detail in the next example.

Figure 4 shows Poincaré sections of globally chaotic motions around all equilibrium positions resulting from the period-doubling mechanism of the three-period motion. Here the forcing amplitude was fixed to 0.7, the forcing frequencies took the following values: (4a) $\omega = 3.500$E3, (4b) $\omega = 3.480$E3, (4c) $\omega = 3.465$E3, (4d) $\omega = 3.460$E3, (4e) $\omega = 3.450$E3, (4f) $\omega = 3.430$E3, (4g) $\omega = 3.420$E3, (4h) $\omega = 3.400$E3.

A three-period motion is visualized through three points in the Poincaré sections (Figure 4a), by reducing $\omega$ the period of the motion doubles to 6, 12, 24 (Figures 4b, 4c, and 4d). The period-doubling mechanism continues and one get chaotic motions around each point in the Poincaré section, until finally a globally chaotic motion results (Figure 4h).

Figure 5 shows Poincaré sections to visualize the period-doubling cascades to chaos due to soft-spring characteristics around one of the equilibrium positions (locally chaotic). The forcing frequency was changed between (4.0E3–4.3E3) while the forcing amplitude was fixed to 0.7: (5a) $\omega = 4.30$E3, (5b) $\omega = 4.20$E3, (5c) $\omega = 4.15$E3, (5d) $\omega = 4.12$E3, (5e) $\omega = 4.05$E3, (5f) $\omega = 4.00$E3.

### 6.2. Chaotic Motion of Shallow Arches

Finite element simulations of the nonlinear dynamics of simply supported and clamped shallow arches are considered in this section.

The first example is a simply supported shallow arch having its hysteresis region of the statically calculated displacement-load diagram around zero, thus a preloading of the arch is not needed. Otherwise a preloading of the arch by a constant load lets us reach a region of more than one equilibrium position. The main differences to the buckled Euler beam are: (1) the potential of the equilibrium positions of the arch is in general not symmetric and includes even and odd nonlinearities, and (2) inertial stress distributions are absent. A point excitation is assumed to act in the middle of the arch. The model with its corresponding data is illustrated

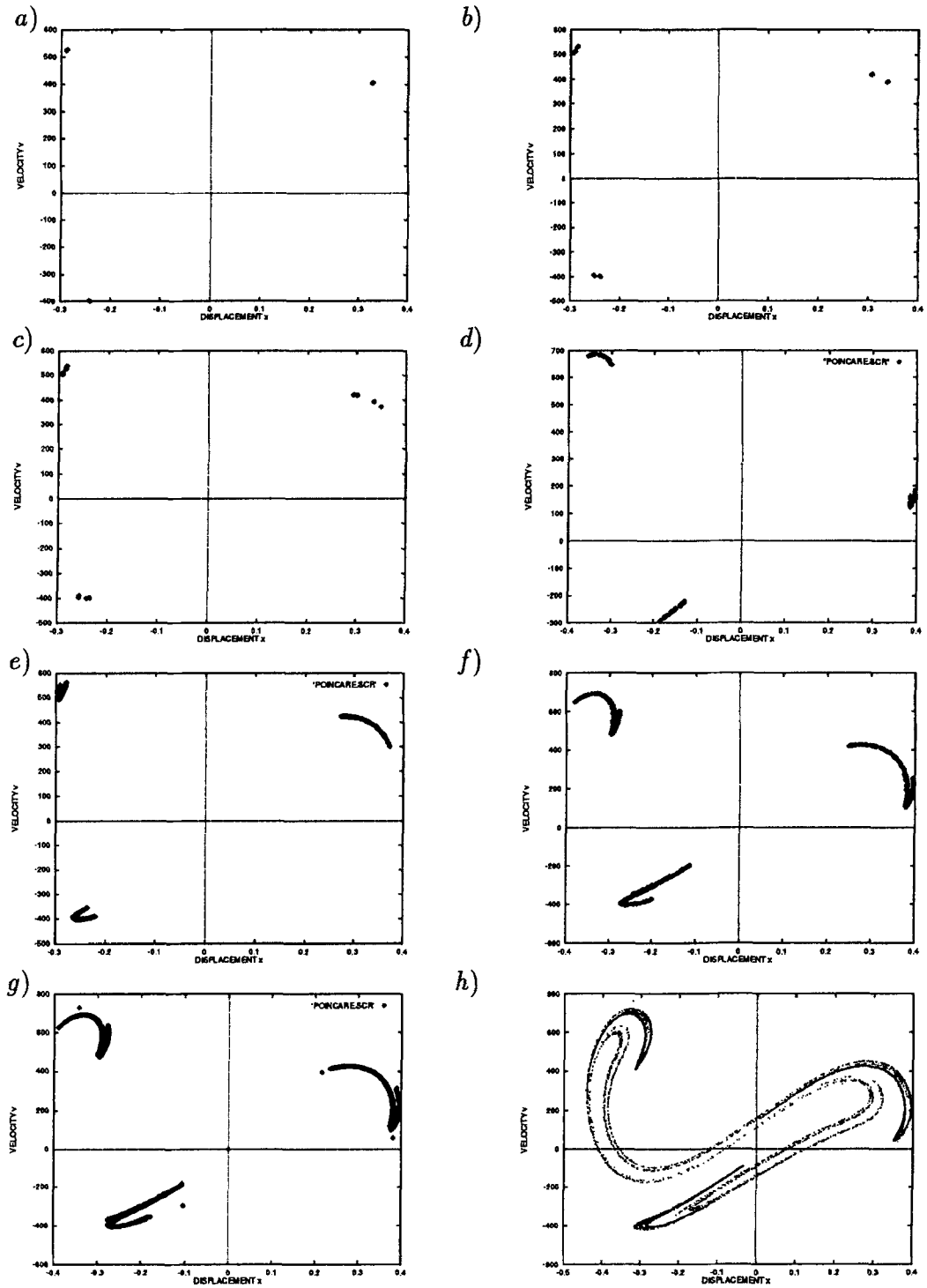


*Figure 4.* Period-doubling of the three-period motion leading to a global chaotic motion. (a) Three-period motion. (b) (2 × 3)-period motion. (c) (4 × 3)-period motion. (d) (8 × 3)-period motion. (e) A very long period. (f) and (g) Chaos due to the period-doubling. (h) Globally chaotic.

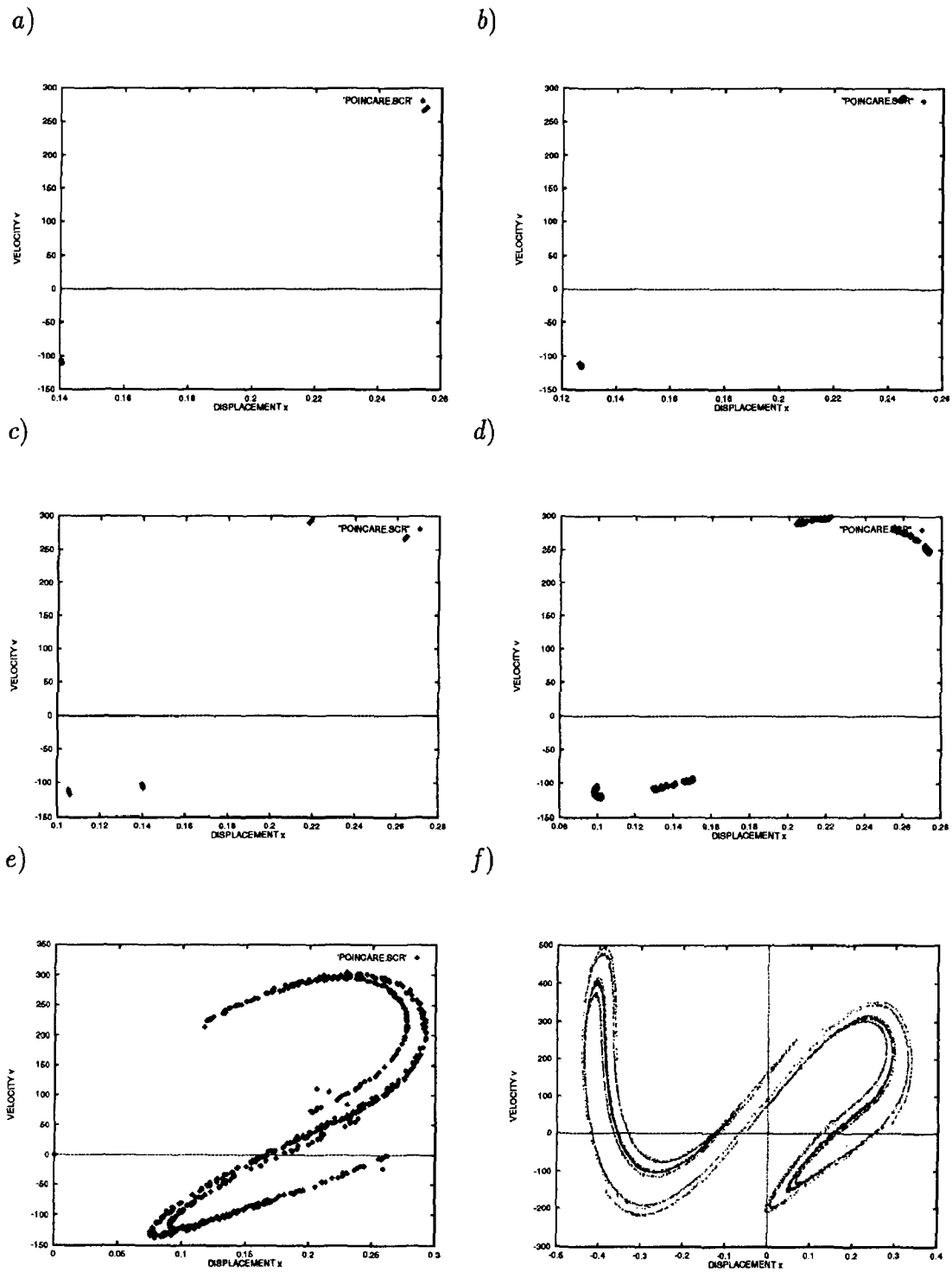


*Figure 5.* Period-doubling of motion around one of the local equilibria leading to a local chaotic motion. (a) and (b) Two-period motion. (c) Four-period motion. (d) large period motion. (e) Locally chaotic. (f) Globally chaotic due to symmetry.

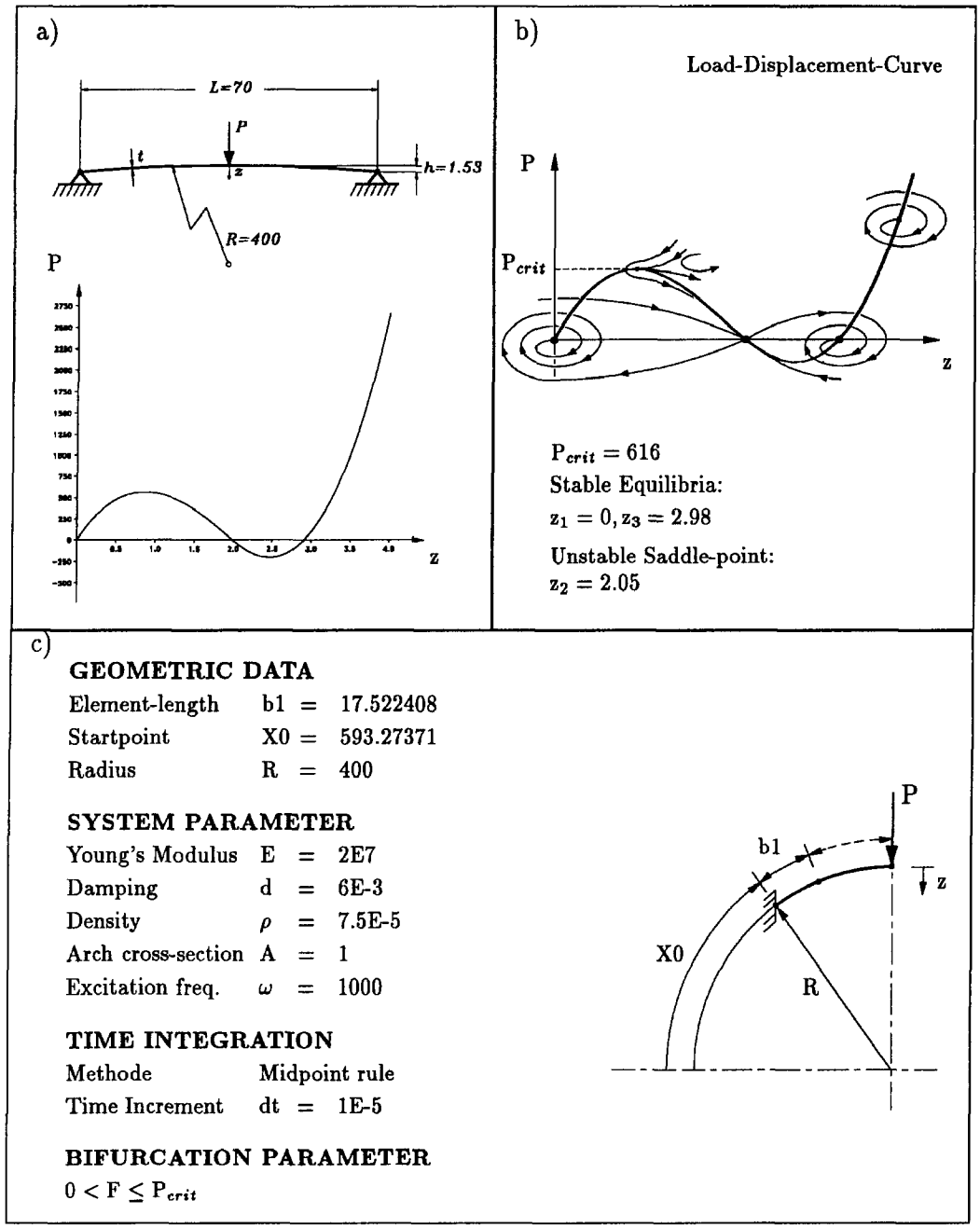


*Figure 6.* The geometry, the data, and the load-displacement diagram of the simply supported shallow arch.

in Figure 6. Since the two stable static equilibria $z_1$ and $z_3$ are sinks in the dynamical case (i.e. having complex eigenvalues with negative real parts in the linearized motion of the low dimensional Galerkin projection), the unstable point $z_2$ is of saddle type; i.e. having stable and unstable manifolds where the unstable ones end into the stable equilibria $z_1$ and $z_3$ (see Figure 6b). A harmonic excitation would convert the stable and unstable equilibrium positions into stable and unstable cycles having stable and unstable nonlinear manifolds [2, 3, 24]. A

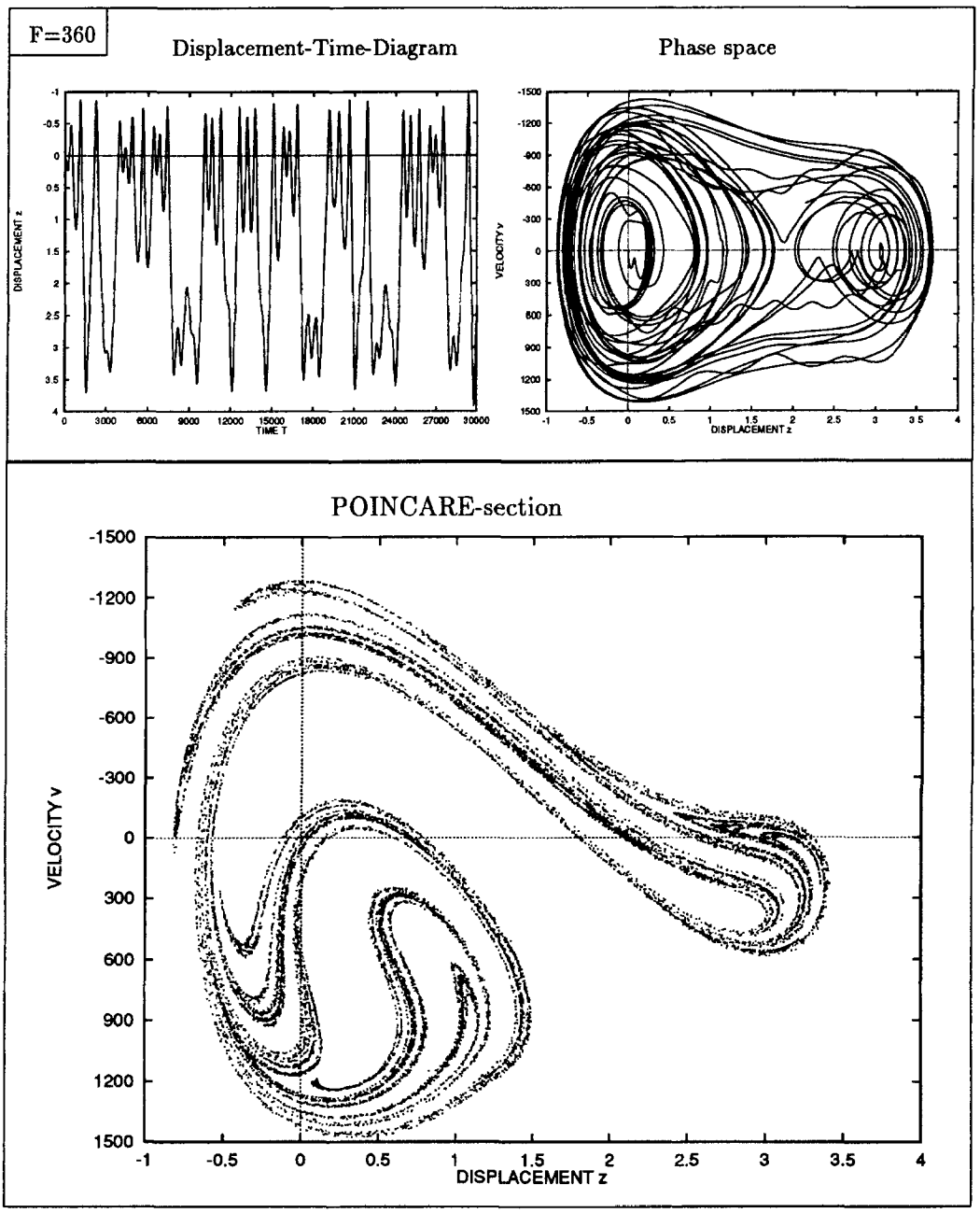


*Figure 7.* Chaotic attractor; Poincaré section with the corresponding $(z-t)$- and $(v-x)$-plots. $F = 360$, frequency $= 1000$.

low dimensional Melnikov analysis that finds the touch of the stable and unstable manifolds (*homoclinic point*) causing Horseshoe-like dynamics and chaotic motion (see, e.g., [25]) in the case of the shallow arch can be found in [12, 13].

Through varying the forcing amplitude of a harmonically point-excitation different kinds of nonlinear vibrations (Figure 7, chaotic vibration) can exist for a large scale. Period-doubling

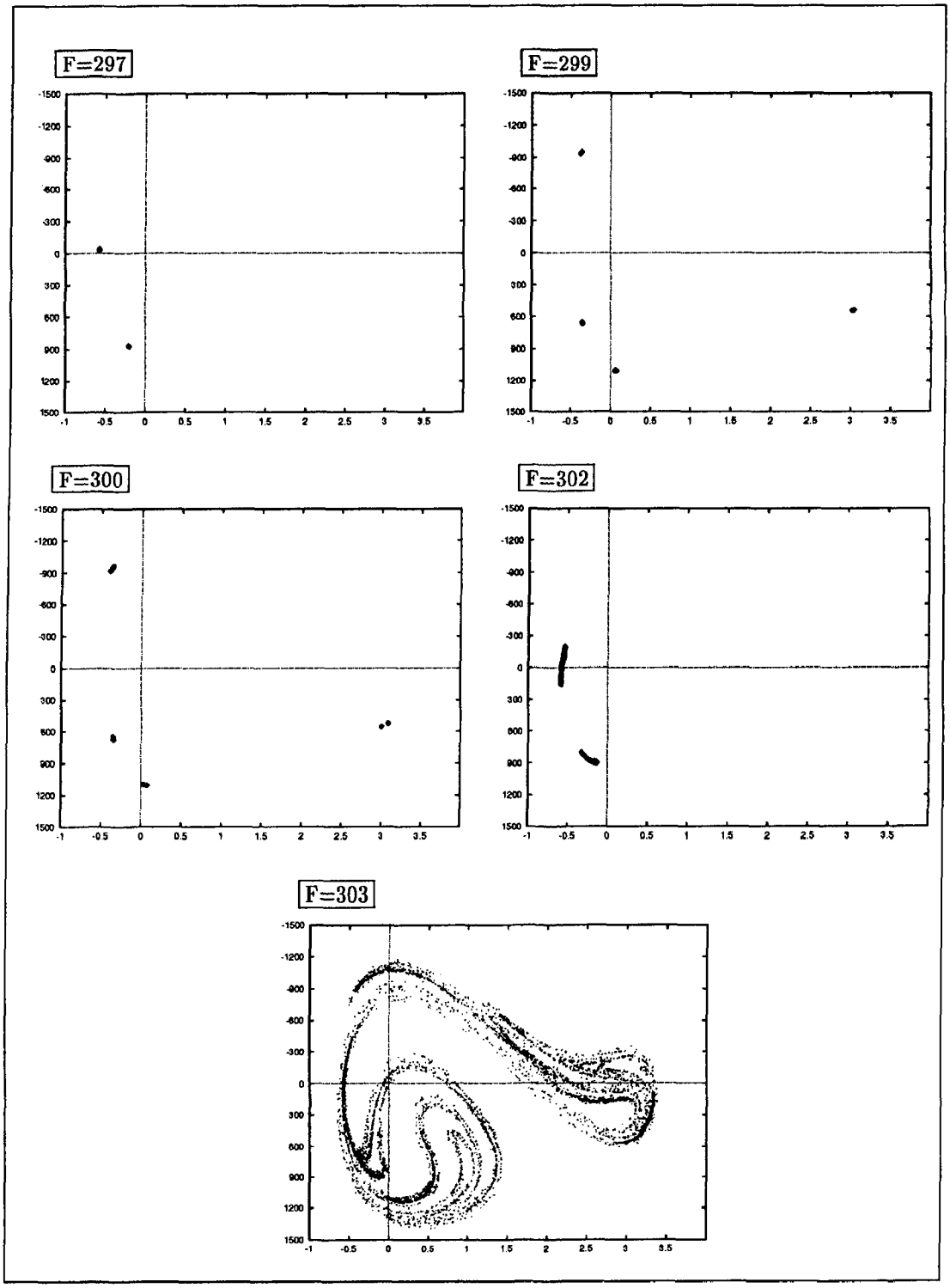


*Figure 8.* Two different bifurcation cascades leading to local and global chaotic motions ($F = 302$, $F = 303$) of the arch, which may coexist.

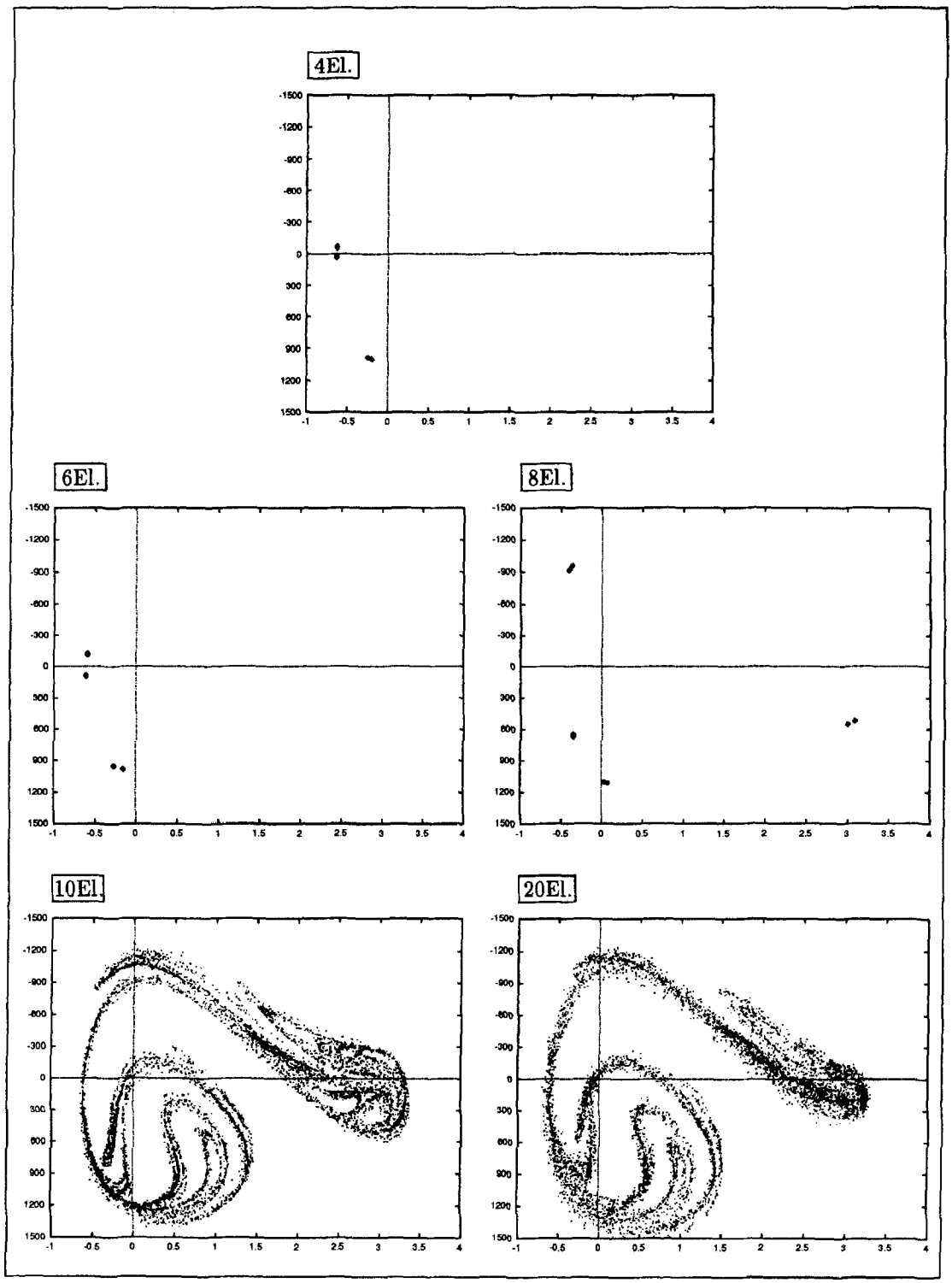


*Figure 9.* Poincaré sections for different used numbers of finite element. After 10 elements the chaotic motion became robust. El. = Element.

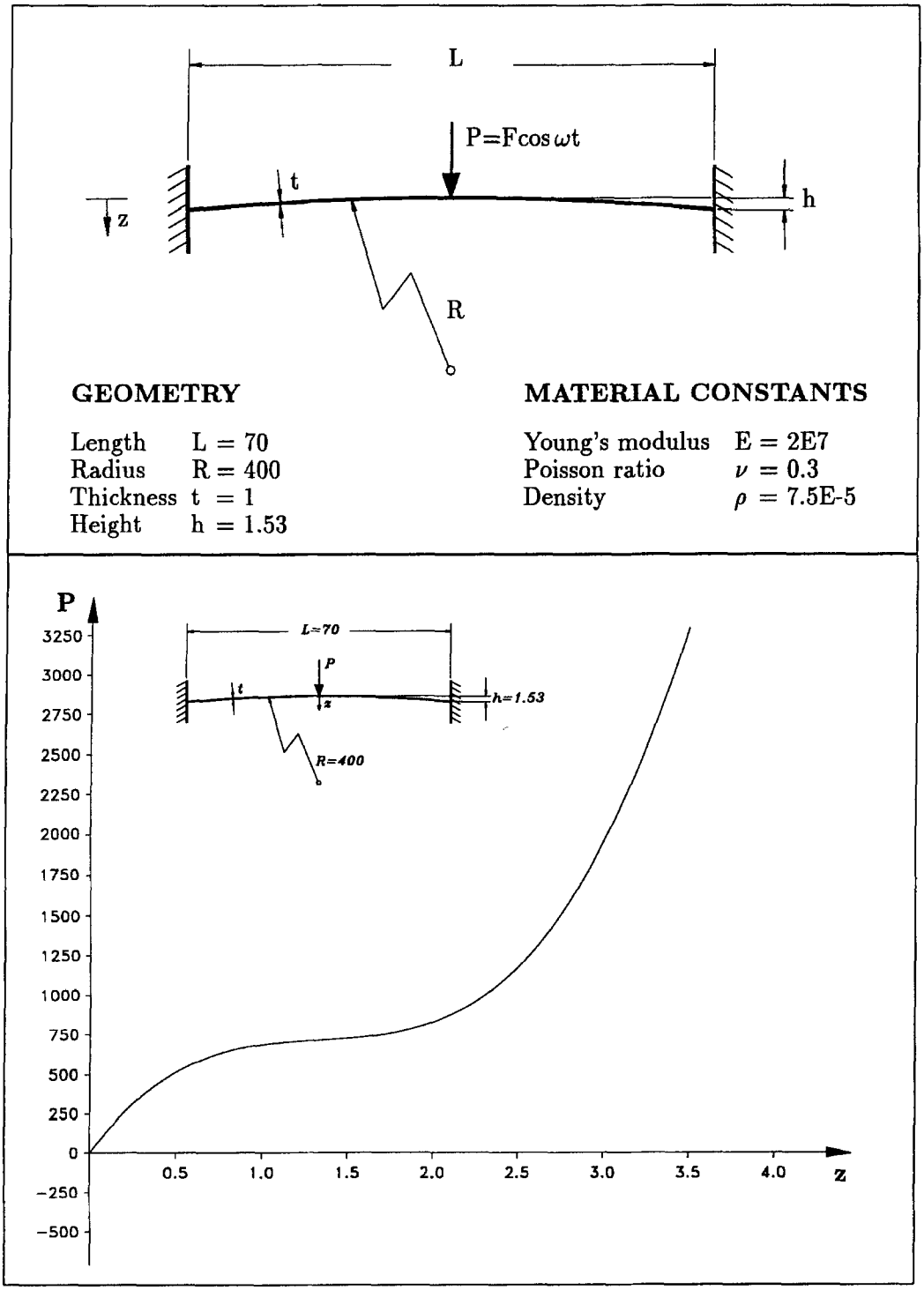


*Figure 10.* The geometry of the clamped shallow arch and its corresponding load-displacement diagram.

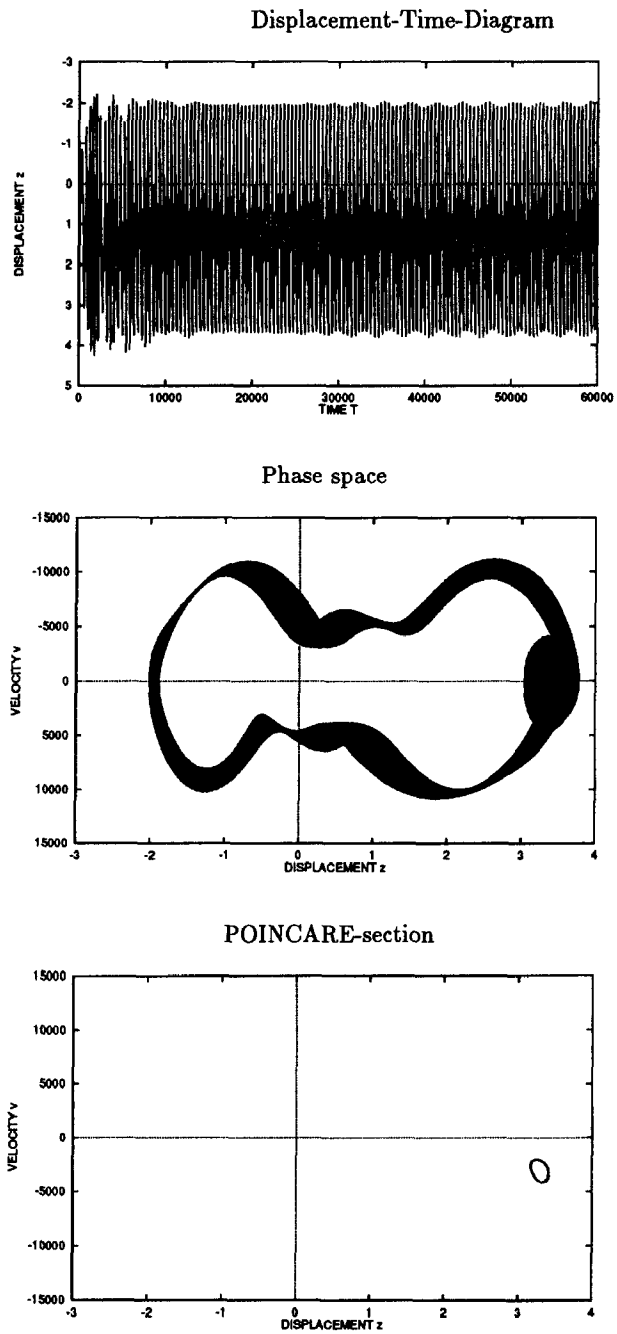


*Figure 11.* Modulated motion of the arch (quasi-periodic).

of odd and even subharmonics are possible. Even the coexistence of two different period-doubling cascades which lead to various chaotic motions can be observed; one of them is local around one equilibrium position and the other one is global around all equilibria (Figure 8).

The threshold force of the chaotic motion can be varied with the number of the used modes which approximate the motion [5, 18]. Figure 9 shows the influence of the number of the used

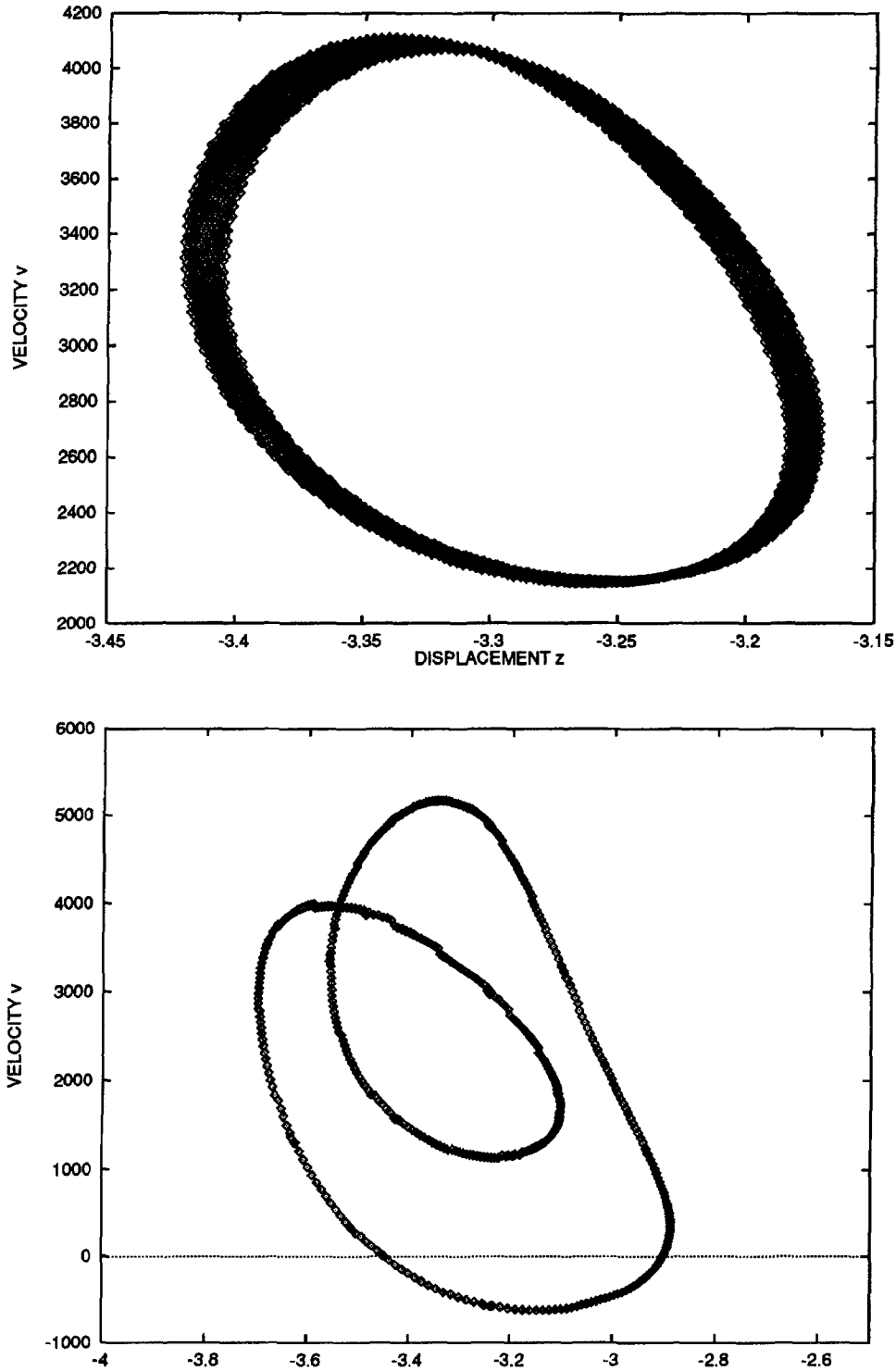


*Figure 12.* Poincaré sections of the quasi-periodic motion of different order which may lead to a chaotic modulated motion of the arch (period-doubling of the second mode).

finite elements in the calculation on the start point of a chaotic motion. For more than ten elements the chaotic motion became robust.

The second example is a clamped shallow arch (Figure 10) which has just one equilibrium position. For a specific set of parameters a second mode enters the dynamics, and due to resonance and coupling of modes the resultant motion is a modulated one. (Here quasi-periodic motion visualized through a ring in the Poincaré section; the frequencies are incommensurable (Figure 11).) The period-doubling of the second mode is also possible (Figure 12) which may end up into a chaotic modulated motion.

## 7. Concluding Remarks

In this paper the nonlinear dynamics and chaotic motion of geometrically exact rods and arches, modeled directly as a one-dimensional nonlinear manifold (Cosserat line), are considered. The finite element method is applied for the numerical simulation. The configuration space of the rod consists of displacements and rotations. A hybrid finite element was developed in order to avoid ill-conditioning and locking phenomena. For the time integration the symplectic midpoint-rule has been used.

Basic advantages of the approach are the natural coupling of rotations and the possible use of a large number of modes where the influence of the passive modes are considered in a natural way. It was shown that the inclusion of higher order modes by the use of sufficient number of finite elements does influence the threshold force and the fine structure of the chaotic attractor.

The present approach can be generalized to encompass geometrically exact shells. First steps in this direction are made in [16, 17]. The significance of the approach lies in the act that the standard Galerkin method, which seems to work well for one-dimensional structures, may fail in complicated structures explicitly shells where the passive modes have remarkable contribution to shell dynamics and buckling and may influence the post critical behavior of the shell as well.

Here, the time integration scheme becomes of special interest. Recent promising developments are the consideration of what is called energy-momentum preserving integration schemes [20, 21]. The methods, however, must be modified in order to be applicable to nonlinear configuration spaces. These aspects and the dynamics of geometrically exact shells are addressed in [18] to which the reader is referred.

## References

1. Antman, S. S., 'Kirchhoff problem for nonlinearly elastic rods', *Quarterly Journal of Applied Mathematics* **32**, 1974, 221–240.
2. Argyris, J., Faust, G., and Haase, M., 'An adventure into chaos', *Computer Methods in Applied Mechanics and Engineering* **91**, 1991, 997–1091.
3. Guckenheimer, J. and Holmes, P. J., *Nonlinear Oscillations, Dynamical Systems and Bifurcations of Vector Fields*, Springer-Verlag, New York, 1983.
4. Holmes, P. J., 'A nonlinear oscillator with a strange attractor', *Philosophical Transactions of the Royal Society of London, Series A* **292**, 1979, 419–448.
5. Tang, D. M. and Dowell, E. H., 'On the threshold force for chaotic motions for a forced buckled beam', *ASME Journal of Applied Mechanics* **55**, 1988, 190–196.
6. Marsden, J., *Lectures on Mechanics*, London Mathematical Society, Lecture Note Series 174, Cambridge University Press, 1993.
7. Moon, F. C. and Holmes, P., 'A magnetoelastic strange attractor', *Journal of Sound and Vibration* **65**, 1979, 276–296.

8. Moon, F. C. and Shaw, S. W., 'Chaotic vibrations of a beam with nonlinear boundary conditions', *International Journal of Non-Linear Mechanics* **18**, 1983, 465–477.
9. Nayfeh, A. H. and Balachandran, B., 'Modal interactions in dynamical and structural systems', *Applied Mechanics Review* **42**, 1989, S175–S201.
10. Maewal, A., 'Chaos in a harmonically excited elastic beam', *ASME, Journal of Applied Mechanics* **53**, 1986, 625–632.
11. Mook, D. T., Plant, R. H., and HaQuang, N., 'The influence of an internal resonance on non-linear structural vibrations', *Journal of Sound and Vibration* **102**, 1985, 473–492.
12. Namachchivaya, N. S. and Doyle, M. M., 'Chaotic motion of a shallow arch', in *Proceedings of the 29th Structures, Structural Dynamics and Materials Conference*, Williamsburg, VA, 1988, pp. 198–209.
13. Tien, W.-M. and Namachchivaya, N. S., 'Non-linear dynamics of a shallow arch under periodic excitation', *International Journal of Non-Linear Mechanics* **29**, 1994, 349–386.
14. Reissner, E., 'On finite deformations of space curved beams', *Journal of Applied Mathematics and Physics* **32**, 1981, 734–744.
15. Sansour, C. and Bednarcyck, H., 'The Cosserat surface as shell model, theory and finite element formulation', *Computer Methods in Applied Mechanics and Engineering* **120**, 1995, 1–32.
16. Sansour, C. and Sansour, J., 'Dynamical formulation of shells at finite rotations with corresponding finite element computations of chaotic vibrations', in *Proceedings of the Congress of Applied Mechanics in the Americas 2*, Buenos Aires, Argentina, L.E. Godoy et al. (eds.), 1995, pp. 309–314.
17. Sansour, C. and Sansour, J., 'Eine dynamische Formulierung einer Schalentheorie mit Drill-Freiheitsgraden und zugehörigen Finite-Elemente-Berechnungen', *Zeitschrift für angewandte Mathematik und Mechanik, ZAMM* **75**, 1995, 67–68.
18. Sansour, C., Wriggers, P., and Sansour, J., 'On the dynamics of shells using the Cosserat model and a new time integration scheme', in preparation.
19. Simo, J. C., 'A finite strain beam formulation. The three dimensional dynamic problem. Part I', *Computer Methods in Applied Mechanics and Engineering* **49**, 1985, 55–70.
20. Simo, J. C. and Tarnow, N., 'The discrete energy-momentum method. Conserving algorithms for nonlinear elastodynamics', *Zeitschrift für angewandte Mathematik und Physik, ZAMP* **43**, 1992, 757–792.
21. Simo, J. C. and Tarnow, N., 'A new energy and momenten conserving algorithms for the nonlinear dynamics of shells', *International Journal of Numerical Mathematics in Engineering* **37**, 1994, 2527–2549.
22. Simo, J. C., Tarnow, N., and Wong, K. K., 'Exact energy-momentum conserving algorithms and symplectic schemes for nonlinear dynamics', *Computer Methods in Applied Mechanics and Engineering* **100**, 1992, 63–116.
23. Simo, J. C., Hjelmstad, K. H., and Taylor, R. L., 'Numerical formulations for the elasto-viscoplastic response of beams accounting for the effect of shear', *Computer Methods in Applied Mechanics and Engineering* **42**, 1984, 301–330.
24. Thompson, J. M. T. and Stewart H. B., *Nonlinear Dynamics and Chaos*, Wiley, Chichester, 1986.
25. Wiggins, S., *Introduction to Applied Nonlinear Dynamical Systems and Chaos*, Springer-Verlag, New York, Berlin, 1991.